



A Discussion About Two-Phase Flow Pressure Drop in Proton Exchange Membrane Fuel Cells

Mehdi Mortazavi^a, Mahbod Heidari^b, and Seyed A. Niknam^c

^aDepartment of Mechanical Engineering, Western New England University, Springfield, Massachusetts, USA; ^bInstitute of Chemical Sciences and Engineering, Ecole Polytechnique Federale de Lausanne (EPFL), Lausanne, Switzerland; ^cDepartment of Industrial Engineering, Western New England University, Springfield, Massachusetts, USA

ABSTRACT

A proton exchange membrane (PEM) fuel cell produces water during its operation which results in a liquid-gas two-phase flow within its flow channels. Because the length scales associated with flow channels are small, the two-phase flow in PEM fuel cell is mainly dominated by capillary forces. These capillary forces tend to hold droplets within the channels which eventually increase the pressure drop along the flow channels. The two-phase flow pressure drop along the flow channel can reveal information about the amount of liquid water accumulation. Therefore, a precise two-phase flow pressure drop model that can accurately predict the pressure drop in PEM fuel cell flow channels can be beneficial in estimating the amount of water content in flow channels. In the current study, liquid-gas two-phase flow pressure drops were measured in an ex-situ test section with liquid water and air flowing within the range of PEM fuel cell flow conditions. The measured pressure drops were then compared with nine existing pressure drop models developed for minichannels. Qualitative and quantitative comparisons are provided to compare the prediction capability of the models. Also, a discussion about capillary-scale two-phase flow systems and suggestions to improve prospective two-phase flow pressure drop models is provided.

Introduction

Proton exchange membrane (PEM) fuel cells have received attention as efficient and pollutant-free energy conversion devices. They generate electricity through electrochemical reactions by utilizing hydrogen and oxygen within the electrodes. These reactions produce water and heat as byproducts. A robust fuel cell operation requires an even and steady supply of reactants across the electrodes. While some portion of the produced water is beneficial for fuel cell operation as it hydrates the proton conductive membrane, an excess amount of liquid water can occupy open pores of the gas diffusion layer (GDL). The GDL is a microporous layer, which serves different purposes including providing a uniform transport of reactants to the catalyst layer, removing excess water from the membrane, mechanically protecting the fragile membrane, and providing electrical conductivity between the electrodes and current collectors. A successful GDL design has been reported to

have a significant contribution toward improved water balance within the cell [1–5].

Transporting an excess amount of liquid water to a GDL can eventually obstruct the flow of reactants to the catalyst layer. This causes GDL flooding, which adversely impacts PEM fuel cell performance [6–8]. Liquid water can also enter flow channels by emerging as droplets at some preferential locations [9–12]. Water transport mechanisms in PEM fuel cell flow channels were classified by Zhang et al. [13]. It was observed that when both the water production rate and the superficial gas velocity are low, water drains from inside the channel by spreading over hydrophilic channel walls and transports through the corners, forming corner flow. The fluid's superficial velocity is its bulk velocity within the cross-sectional area of the flow channel. For a moderate water production rate, corner flow may not be adequate to remove liquid water, and therefore, it changes to annular film flow. Finally, for high water production rate, the annular

CONTACT Dr. Mehdi Mortazavi  mehdi.mortazavi@wne.edu  Department of Mechanical Engineering, Western New England University, 1215 Wilbraham Road, Springfield, MA 01119.

Color versions of one or more of the figures in the article can be found online at www.tandfonline.com/uhte.

© 2019 Taylor & Francis Group, LLC

Nomenclature

Bo	Bond number, $Bo = (\rho_f - \rho_g)g \left(\frac{D_h}{2}\right)^2 / \sigma$ (-)	Greek symbols	
C	Parameter in Lockhart-Martinelli correlation (-)	Δ	Difference (-)
$(\frac{dp}{dz})_{hom}$	Two-phase pressure gradient predicted by the homogeneous model by the use of average viscosity based on Ref. [53] (Pa/m)	α	Void fraction (-)
D_h	Hydraulic diameter of channels, $4wh/(2w + 2h)$ (m, unless otherwise noted)	β	Channel aspect ratio ($\beta < 1$)
Fr	Froude number (-)	η	Corner half-angle (°)
f	friction factor (-)	ξ	Percentage of data points predicted within $\pm 50\%$ (-)
g	Gravitational acceleration (m/s ²)	θ	Percentage of data points predicted within $\pm 30\%$ (-)
G	Mass flux (kg/m ² s)	θ_s	Static contact angle (°)
GDL	Gas diffusion layer (-)	ϵ	Dimensionless number used in Refs. [28, 39]
h	Channel height (m)	λ	Mean absolute percentage error (-)
j_f	Superficial liquid velocity (m/s)	μ	Dynamic viscosity (N·s/m ²)
j_g	Superficial gas velocity (m/s)	ρ	Density (kg/m ³)
La	Non-dimensional Laplace constant (-)	σ	Surface tension (N/m)
L	Characteristic length (m, unless otherwise noted)	ϵ	Inverse of Laplace number (-)
L_c	Capillary length (m, unless otherwise noted)	ψ	Capillary number (-)
l_e	Entrance length (m)	Ω	Homogeneous pressure drop correction factor (-)
MAPE	Mean absolute percentage error (-)	φ^2	Two-phase flow frictional multiplier (-)
N	Number of data points (-)	φ_i	channel inclination angle (°)
N_{conf}	Confinement number (-)	ω	Percentage of data points predicted within $\pm 10\%$ (-)
P	Pressure (Pa)		
P_c	Critical pressure (Pa)	Subscripts	
PEM	Proton exchange membrane (-)	A	accelerational
PTFE	Polytetrafluoroethylene (-)	exp	experimentally obtained
R^2	Coefficient of determination (-)	F	frictional
Re	Reynolds number (-)	G	gravitational
Re_f	Reynolds number based on superficial liquid velocity (-)	TP	two-phase
Re_g	Reynolds number based on superficial gas velocity (-)	f	saturated liquid
Re_{D_h}	Reynolds number based on hydraulic diameter	g	saturated vapor
STD	Pressure standard deviation (Pa)	fo	liquid only
v	Specific volume (m ³ /kg)	go	vapor only
w	Channel width, (m)	hom	homogeneous
We	Weber number, $We = \frac{G^2 D_h}{\sigma \rho}$, (-)	pred	predicted
WFR	Water flow rate ($\mu\text{l/h}$)		
x	Mass flow quality, coordinate (-)		
X	Lockhart-Martinelli parameter (-)		
z	Streamwise coordinate (m)		

film flow may change to slug flow within the flow channels. The latter may cause channel flooding which can ultimately lower the performance of the cell [14–16]. Another two-phase flow pattern may occur in PEM fuel cell flow channels, which requires high superficial gas velocities. In this case, the shear force from the gas stream can detach the water droplets from the surface of the GDL, which forms mist flow. Mortazavi and Tajiri [17] studied liquid water droplet detachment from the surface of the GDL caused by shear force from the gas stream. In addition, enhanced water removal techniques from the flow channels of PEM fuel cells have been proposed by externally exciting water droplets around their natural frequencies [18, 19].

The current study focuses on an area with little published literature, liquid-gas two-phase adiabatic flow with low mass fluxes ($G_{TP} < 10 \text{ kg/m}^2\text{s}$) in mini-channels with GDLs as their side walls. Liquid-gas two-phase flow pressure drops were experimentally obtained while air and water were directly supplied into the channels. This resembles liquid-gas two-phase flow condition in PEM fuel cell flow channels. The experimentally obtained liquid-gas two-phase flow pressure drops were then compared with different two-phase flow pressure drop models proposed in literature. The motivation of this study was to identify the most accurate two-phase flow pressure drop model with the highest prediction capability for the application of PEM fuel cell. Identifying an accurate

pressure drop model can be used to predict liquid water content within the PEM fuel cell flow channels by measuring the pressure drop. The quantitative and qualitative comparison between experimentally obtained pressure drops and models are followed with a discussion about capillary-scale two-phase flow. Because the liquid-gas two-phase flow in PEM fuel cell flow channels is dominated by capillarity, the parameters describing this phenomenon should be incorporated into the pressure drop models. These parameters include surface tension, contact angle, and geometry of the channel which are discussed in the corresponding sections. Therefore, the objectives of this study can be itemized as:

1. Collect liquid-gas two-phase flow pressure drop relevant to PEM fuel cell flow conditions.
2. Compare experimentally obtained pressure drop values with several models published in literature to identify the most accurate model. Both separated flow models and homogeneous equilibrium models were considered in evaluation.
3. Provide discussion about capillary-scale two-phase flow in PEM fuel cells and suggestions to improve prospective models.

Two-phase flow pressure drop

Despite the well-understood single-phase flow pressure drop, the liquid-gas two-phase flow pressure drop is not thoroughly identified at different ranges of flow conditions. Although two-phase flow in PEM fuel cell has been the subject of several studies [20–25], an accurate prediction of two-phase flow pressure drop in PEM fuel cell flow channels is still a challenge for researchers. The liquid-gas two-phase flow pressure gradient includes frictional, gravitational, and accelerational pressure gradients:

$$\left(-\frac{dP}{dz}\right)_{TP} = \left(-\frac{dP}{dz}\right)_{TP,F} + \left(-\frac{dP}{dz}\right)_{TP,G} + \left(-\frac{dP}{dz}\right)_{TP,A} \quad (1)$$

The accelerational pressure gradient, $\left(-\frac{dP}{dz}\right)_{TP,A}$, is expressed as follows:

$$\left(-\frac{dP}{dz}\right)_A = G^2 \frac{d}{dz} \left[\frac{v_g x^2}{\alpha} + \frac{v_f (1-x)^2}{(1-\alpha)} \right] \quad (2)$$

In this equation x is the mass flow quality which is defined as follows:

$$x = \frac{G_g}{G_g + G_f} \quad (3)$$

and α defines the amount of gas holdup within the liquid flow. Different techniques have been suggested to measure α [26–30].

For the application of PEM fuel cell, the accelerational pressure gradient is negligible compared to the overall two-phase flow pressure gradient and therefore it can be ignored. The gravitational pressure gradient for an inclined channel with an inclination angle of φ_i is defined as

$$\left(-\frac{dP}{dz}\right)_G = [\alpha \rho_g + (1-\alpha) \rho_f] g \sin \varphi_i \quad (4)$$

The gravitational pressure gradient term will be zero for a horizontal channel. The gravitational pressure gradient in PEM fuel cell flow channels is negligible since the gravitational effects are trivial compared to the surface tension effects. As accelerational and gravitational pressure gradients for the minichannels of PEM fuel cells are negligible, only the frictional pressure gradient term remains on the right-hand side of the Eq. (1). Depending on how each of the phases is treated, the frictional two-phase flow pressure drop can be predicted based on two different methods. In the first method, the two-phase flow is treated as a pseudo single-phase fluid with properties weighted by the quality. This method is referred to as the homogeneous equilibrium model, which has proven to be more precise at higher mass qualities [31, 32]. The homogeneous equilibrium model is also known as the zero-slip model because it is assumed that both phases are traveling at the same speed. According to this model, the frictional two-phase flow pressure gradient can be calculated by

$$\left(-\frac{dP}{dz}\right)_{TP,F} = \frac{2f_{TP}G^2}{D_h \rho_{TP}} \quad (5)$$

where f_{TP} is the two-phase friction factor and is a function of the two-phase Reynolds number, Re_{TP}

$$f_{TP} = \begin{cases} \frac{16}{Re_{TP}} & \text{for } Re_{TP} < 2,000 \\ 0.079 Re_{TP}^{-0.25} & \text{for } 2000 \leq Re_{TP} < 20,000 \\ 0.046 Re_{TP}^{-0.2} & \text{for } Re_{TP} \geq 20,000 \end{cases} \quad (6)$$

The two-phase Reynolds number can be calculated by

$$Re_{TP} = \frac{GD_h}{\mu_{TP}} \quad (7)$$

Triplett et al. [33] studied the accuracy of the homogeneous flow model and observed that while this method can properly predict the two-phase flow pressure drop for bubbly and slug flows, it shows less accuracy in predicting the pressure drop in the

slug-annular and annular flow patterns. In the second method, the two-phase flow pressure drop is correlated to the single-phase pressure drop by multiplying by a two-phase flow frictional multiplier. This technique, which is referred to as the separated flow model, was introduced by Lockhart and Martinelli in 1949 [34]. According to this model, the frictional two-phase flow pressure gradient is calculated by

$$\left(-\frac{dP}{dz}\right)_{TP,F} = \phi_f^2 \left(-\frac{dP}{dz}\right)_f \quad (8)$$

Where ϕ_f^2 is the two-phase frictional multiplier based on the liquid. Wang et al. [35] studied the two-phase flow patterns of different refrigerants in a 6.5-mm diameter tube and observed that the two-phase frictional multiplier depends on the flow pattern.

Chisholm [36] introduced the Chisholm parameter, C , which is used to calculate the frictional multiplier:

$$\phi_f^2 = \frac{\left(-\frac{dP}{dz}\right)_{TP}}{\left(-\frac{dP}{dz}\right)_f} = 1 + \frac{C}{X} + \frac{1}{X^2} \quad (9)$$

where X is the Martinelli parameter, defined as:

$$X = \left[\left(-\frac{dP}{dz}\right)_f / \left(-\frac{dP}{dz}\right)_g \right]^{1/2} \quad (10)$$

The concept behind Eq. (9) is that the two-phase flow pressure gradient is equal to the sum of the liquid phase pressure gradient, the gas phase pressure gradient, and the interaction between liquid and gas phase pressure gradient:

$$\left(-\frac{dP}{dz}\right)_{TP} = \left(-\frac{dP}{dz}\right)_f + \left(-\frac{dP}{dz}\right)_g + C \left[\left(-\frac{dP}{dz}\right)_f \left(-\frac{dP}{dz}\right)_g \right]^{1/2} \quad (11)$$

The Chisholm parameter, C , represents the amount of interaction between the liquid and gas phases. Chisholm [36] proposed four different values for this parameter, depending on the liquid and gas flow regimes. Table 1 lists the values of parameter C proposed by Chisholm [36]. The nine two-phase flow pressure drop models that were assessed in this study are listed in Table 2 [28, 37–44]. Models developed for channel sizes close to PEM fuel cell flow channels were selected for this purpose. Also, both separated flow models and homogeneous equilibrium models were selected. A comprehensive review of two-phase flow pressure drop models was previously performed by Mortazavi and Tajiri [45].

Table 1. Values of Chisholm parameter C [36].

Two-phase flow characteristics	Chisholm's parameter
Laminar liquid-laminar gas	5
Turbulent liquid-laminar gas	10
Laminar liquid-turbulent gas	12
Turbulent liquid-turbulent gas	21

Experimental setup

Two-phase flow pressure drop measurement

The two-phase flow pressure drop was measured in an ex-situ experimental setup as schematically shown in Figure 1. The setup consists of a high-precision pressure transducer with a 0–500 Pa pressure range (Omega, PX653 02D5V), air flow meters with 100–500 ml/min (Omega, FLR-1003D) and 400–2000 ml/min (Omega, FLR-1005D) flow ranges, two syringe pumps, and a 12-bit National Instrument USB DAQ (USB-6008). Two parallel flow channels were machined on a 0.5-in-thick polycarbonate plate. The flow channels branched off a header (2 mm × 1 mm). The flow channels were 26-cm long, and the pressure drop was measured over the 20-cm length of the channel through 0.396-mm diameter holes in one of the polycarbonate plates. The high-pressure tap was 41 mm downstream of the channel entrance. For the highest air flow rate (air $Re_{D_h} = 385.3$) the entrance length is obtained at 29.6 mm based on the correlation for the laminar flow

$$\frac{l_e}{D_h} = 0.06 Re_{D_h} \quad (12)$$

Therefore, the pressure drop was measured within the fully developed length of the flow. An ethylene propylene diene monomer foam strip was laser cut and inserted in a groove machined around the flow channels for sealing purposes. The polycarbonate plate with machined flow channels was sandwiched with another polycarbonate plate using 16 1/8-in screws, spaced 4 cm apart. In addition to these screws, three small C-clamps were used to tighten the test section to ensure proper sealing. Polytetrafluoroethylene (PTFE) treated Toray carbon paper (TGP-060) was inserted between the two polycarbonate plates. Air was supplied by a compressed-air bottle to the header channel through a 1/8-in PTFE tube at a 45° angle to the header to facilitate air flow along the channels. Deionized water was injected through two 250-μm diameter stainless steel capillaries (Upchurch-U111) into the flow channels. The capillaries inserted into the polycarbonate plate had a 1/16-in outer diameter. The water introduction was directly into the flow channel side rather than from the back side of the

Table 2. Two-phase flow frictional pressure gradient correlations evaluated in the current study.

Author	Equation	Setup
Saisorn and Wongmises [28]	$\left(\frac{dP}{dz}\right)_{TP,F} = \left(\frac{dP}{dz}\right)_f \phi_f^2, \phi_f^2 = 1 + \frac{\epsilon}{X} + \frac{1}{X^2}, \psi = \frac{\mu \mu_L}{\rho_f \sigma}, \epsilon = \frac{\mu_f^2}{\rho_f \sigma D_h},$ $C = 7.599 \times 10^{-3} \epsilon^{-0.631} \psi^{0.005} Re_{fo}^{-0.008}$	$D_h = 0.15\text{--}0.53$ mm air-water
English and Kandlikar [37]	$\left(\frac{dP}{dz}\right)_{TP,F} = \left(\frac{dP}{dz}\right)_g \phi_g^2, \phi_g^2 = 1 + CX + X^2$ <p>For rectangular channel, $C = 5[1 - \exp(-319D_h)]$</p>	$D_h = 1.017$ mm air-water
Mishima and Hibiki [38]	$\left(\frac{dP}{dz}\right)_{TP,F} = \left(\frac{dP}{dz}\right)_f \phi_f^2, \phi_f^2 = 1 + \frac{\epsilon}{X} + \frac{1}{X^2}$ <p>For rectangular channel, $C = 21[1 - \exp(-319D_h)]$</p>	$D_h = 1.95\text{--}8.88$ mm air-deionized water
Lee and Lee [39]	$\left(\frac{dP}{dz}\right)_{TP,F} = \left(\frac{dP}{dz}\right)_f \phi_f^2, \phi_f^2 = 1 + \frac{\epsilon}{X} + \frac{1}{X^2}, \psi = \frac{\mu \mu_L}{\rho_f \sigma},$ $\epsilon = \frac{\mu_f^2}{\rho_f \sigma D_h}, C = A \epsilon^q \psi^r Re_{fo}^s$ <p>For laminar liquid-laminar gas flow $A = 6.833 \times 10^{-8}$, $q = -1.317$, $r = 0.719$, $s = 0.557$ For laminar liquid-turbulent gas flow $A = 6.185 \times 10^{-2}$, $q = 0$, $r = 0$, $s = 0.726$</p> <p>For $Re_f < 2,000$ and $Re_g < 2,000$</p>	$D_h = 0.78\text{--}6.67$ mm air-water
Sun and Mishima [40]	$\left(\frac{dP}{dz}\right)_{TP,F} = \left(\frac{dP}{dz}\right)_f \phi_f^2, \phi_f^2 = 1 + \frac{\epsilon}{X} + \frac{1}{X^2}$ $C = 26 \left(1 + \frac{Re_f}{1000}\right) \left[1 - \exp\left(\frac{-0.153}{0.27 \times La + 0.8}\right)\right]$ $La = (\sigma/g(\rho_f - \rho_g))^{0.5} / D_h$ <p>For $Re_f \geq 2,000$ or $Re_g \geq 2,000$</p>	$D_h = 0.97\text{--}5.45$ mm air, water, refrigerants
Zhang et al. [41]	$\left(\frac{dP}{dz}\right)_{TP,F} = \left(\frac{dP}{dz}\right)_f \phi_f^2, \phi_f^2 = 1 + \frac{\epsilon}{X} + \frac{1}{X^2},$ $C = 1.79 \left(\frac{Re_g}{Re_f}\right)^{0.4} \left(\frac{1-x}{x}\right)^{0.5}$ $\left(\frac{dP}{dz}\right)_{TP,F} = \left(\frac{dP}{dz}\right)_f \phi_f^2, \phi_f^2 = 1 + \frac{\epsilon}{X} + \frac{1}{X^2}, C = 21[1 - \exp(-0.142/La)]$ $La = (\sigma/g(\rho_f - \rho_g))^{0.5} / D_h$	$D_h = 0.0495\text{--}6.25$ mm air-water, refrigerant, ammonia
Hwang and Kim [42]	$\left(\frac{dP}{dz}\right)_{TP,F} = \left(\frac{dP}{dz}\right)_f \phi_f^2, \phi_f^2 = 1 + \frac{\epsilon}{X} + \frac{1}{X^2}, C = 0.227 Re_{fo}^{0.452} X^{-0.32} N_{conf}^{-0.82}$ $N_{conf} = \sqrt{\frac{\sigma}{g(\rho_f - \rho_g) D_h^2}}$	$D_h = 0.244\text{--}0.792$ mm R134a
Friedel [43]	$\left(\frac{dP}{dz}\right)_{TP,F} = \left(\frac{dP}{dz}\right)_f \phi_f^2, \phi_f^2 = (1-x)^2 + x^2 \left(\frac{v_g}{v_f}\right) \left(\frac{\mu_g}{\mu_f}\right)^{0.19} \left(1 - \frac{\mu_g}{\mu_f}\right)^{0.7} Fr_{TP}^{-0.045} We_{TP}^{-0.035}$ $3.24 x^{0.78} (1-x)^{0.224} \left(\frac{v_g}{v_f}\right)^{0.91} \left(\frac{\mu_g}{\mu_f}\right)^{0.19} \left(1 - \frac{\mu_g}{\mu_f}\right)^{0.7} Fr_{TP}^{-0.045} We_{TP}^{-0.035}$ $Fr_{TP} = \frac{G^2}{g D_h \rho_{hom}^2}, We_{TP} = \frac{G^2 D_h}{\sigma \rho_{hom}}, \rho_{hom} = \frac{1}{x v_g + (1-x) v_f}$	$D_h > 4$ mm air-water, air-oil, R12
Chen et al. [44]	$\left(\frac{dP}{dz}\right)_{TP,F} = \left(\frac{dP}{dz}\right)_{hom} \Omega, \left(\frac{dP}{dz}\right)_{hom} = \frac{4 \mu_f G^2}{2 D_{TP}^3}, f_{TP} = \frac{16}{Re_{TP}} \text{ for laminar } Re_{TP} = \frac{G D_h}{\mu_{TP}}$ $\Omega = \frac{0.85 - 0.082 Re_g^{-0.5}}{0.57 + 0.004 Re_g^{0.5} + 0.04 Fr^{-1}} + \frac{80 We^{-1.6} + 1.76 Fr^{0.088} + \ln(Re_g) - 3.34}{1 + \exp(8.5 - 1000 g / \mu)}$ $Fr = \frac{G^2}{g D_h \rho_{hom}}, We = \frac{G^2 D_h}{\sigma \rho_{hom}}$	$D_h = 1\text{--}10$ mm air-water, refrigerant, ammonia

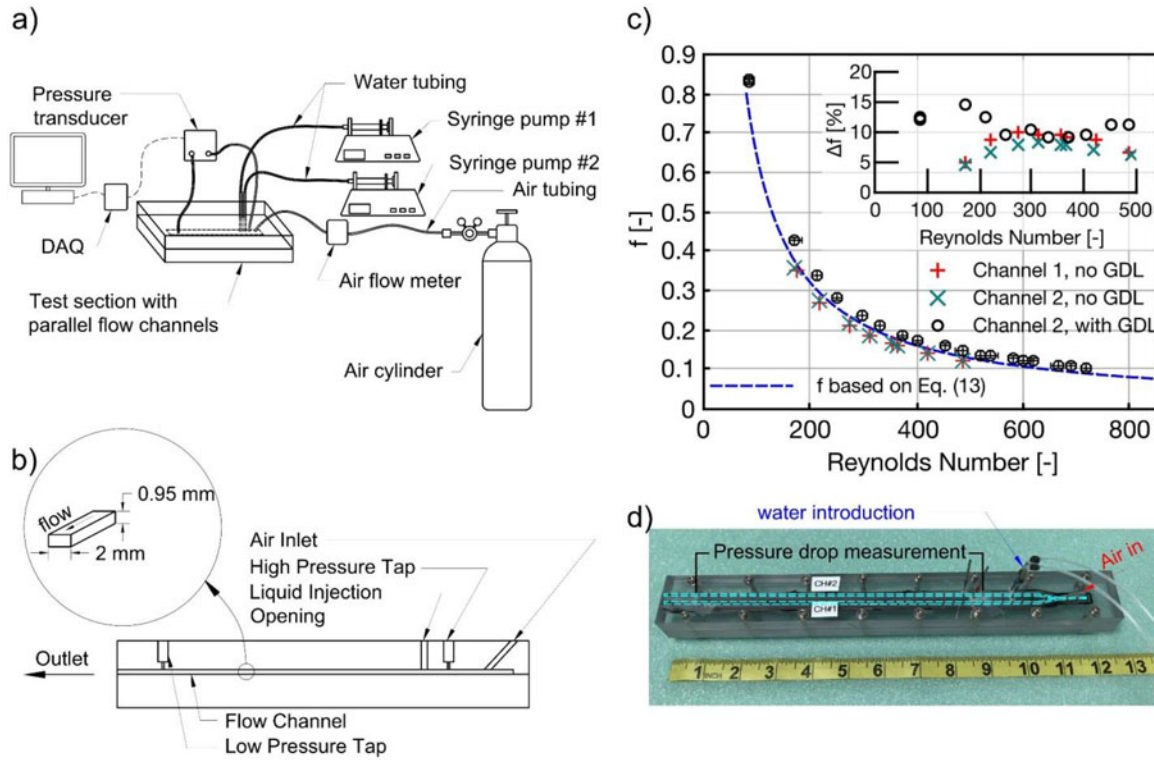


Figure 1. (a) Experimental setup (b) the side view of the test section (c) comparing experimental friction factor obtained from single-phase air flow with laminar flow friction factor correlation, Eq. (13). The figure in the inset shows the difference between the experimental and theoretical friction factor, $\Delta f = \frac{|f_{\text{exp}} - f_{\text{laminar}}|}{f_{\text{laminar}}} \times 100\%$ where f_{laminar} was obtained from Eq. (13) (d) test section, the parallel channels are highlighted with dashed lines.

GDL. This is in contrast with actual PEM fuel cell operation in which water is produced in the electrodes and transported through the GDL to the flow channel.

Water was injected directly into the flow channel in this study to ensure that all the liquid water entered the flow channel without spreading onto the back side of the GDL. However, the GDL was included within the test section to form a porous morphology with a different surface energy on one side of the flow channel. The GDL samples used in this study were treated with PTFE based on the procedure explained in Ref. [46]. To briefly explain, the untreated carbon paper substrates were first dipped into a PTFE emulsion (60 wt.% dispersion in H_2O , ALDRICH) for 10 h. The substrates were then put in a furnace at two steps, first at 120°C for 1 h, and then at 360°C for another hour. Table 3 lists the experimental conditions of this study. The Reynolds number in this table was calculated based on the superficial velocities of air or water and hydraulic diameter of channels. According to Faraday's second law of electrolysis a PEM fuel cell with an active area of 20 cm^2 , current density of 0.6 A/cm^2 , and cathode stoichiometry of 2.5 requires $1.07 \times 10^{-2} \text{ g/s}$ supply air flow rate. This air flow

rate results in an air Reynolds number of 195 in a serpentine design bipolar plate and with 3 parallel channels of $1 \text{ mm} \times 1 \text{ mm}$. Similarly, the water production rate in this cell is $1.12 \times 10^{-3} \text{ g/s}$ which results in a water Reynolds number of 0.41. The air Reynolds number considered in this study was between 96 and 385.3 and the water Reynolds number was between 0.063 and 0.654. This ensures the experimental conditions cover the operating condition of a PEM fuel cell.

Experimental uncertainties

The channel dimensions were measured to be $2 \pm 0.005 \text{ mm}$ and $0.95 \pm 0.002 \text{ mm}$ for the width and the height, respectively. This yields a hydraulic diameter of $D_h = 1.28 \text{ mm}$ and an aspect ratio of $\beta = 0.475$. The uncertainty in the pressure drop measurement was 0.5%, the uncertainty in air flow measurements was between 1.0 and 2.0%, and the uncertainty in liquid flow rate measurement was 2.5%. The pressure drop was measured along $200 \pm 0.5\text{-mm}$ length of the flow channel. Because of the small error in the pressure drop measurement (0.5%), error bars are not included in the pressure plots as adding them will not be noticeable. Similarly, due to small uncertainties in

Table 3. Experiment conditions.

Property	Air	Water	Mixture
Mass flux (kg/m^2s)	1.36-5.44	0.04-0.45	1.56-5.78
Superficial velocity (m/s)	1.13-4.52	$4.40 \times 10^{-5} - 4.53 \times 10^{-4}$	–
Reynolds number (–)	96.0-385.3	0.063-0.654	–
Mass flow quality, $x(-)$	–	–	0.869-0.986

air and water flow rate measurements, the affected properties are not shown with error bars in figures. However, such uncertainties are shown in Figure 1c for friction factor data points calculated for experiments with GDL in the test section.

Experimental procedure

Prior to acquiring data in each run, the air flow rate was regulated with a 1/8-in Swagelok stainless steel low-flow metering valve and the air-flow meter display. Once a stable rate of air was achieved, water injection started and the two-phase flow pressure drop was recorded via a VI code developed in LabView. Each run was conducted for at least 8 min to ensure steady conditions were met. The uniform pressure transducer output also proved this duration was sufficient for the purpose of this study. Between each run, dry nitrogen at a high flow rate was supplied within the flow channels to dry out the liquid water in the flow channels. The single gas phase pressure drop at the beginning of each run was carefully monitored to ensure no liquid water existed in the flow channel at the beginning of each run. All experiments were conducted at atmospheric pressure and room temperature.

Results and discussion

Single-phase pressure drop

To evaluate the accuracy of the test section, the single-phase air pressure drop was measured in both flow channels to calculate the friction factor. Figure 1c shows the calculated friction factor based on the measured pressure drop at different Reynolds numbers. As the air flow rates were in the laminar regime, the calculated friction factors were compared with a fully developed laminar flow friction factor correlation [47]

$$f \cdot Re_{D_h} = 24[1 - 1.3553\beta + 1.9467\beta^2 - 1.7012\beta^3 + 0.9564\beta^4 - 0.2537\beta^5] \quad (13)$$

Friction factors for experiments with and without GDL were obtained. It can be observed from the

figure that channels 1 and 2 show similar friction factors that were both slightly less than the theoretical value. However, the calculated friction factor for channel 2 and with GDL inserted was slightly greater than the predicted friction factor from the laminar regime correlation. This can be due to the GDL intrusion to the flow channel which reduced the cross sectional area of the channel as discussed by St-Pierre [48]. The inset in Figure 1c compares the experimentally obtained friction factors with laminar flow friction factor from Eq. (13).

Comparison of published Two-Phase flow pressure drop models

Figure 2 plots the predicted two-phase flow pressure drops obtained by seven different separated flow models considered in this study [28, 37–42]. The predictions were performed based on 3.0 m/s superficial air velocity and over the full range of mass flow qualities. The prediction based on Friedel [43] and Chen et al. [44] are not shown in this figure because of the large deviation from the experimentally obtained pressure drops as discussed in the next section. All models presented in this figure show a similar trend of decreasing the pressure drop as the mass flow quality increases. This is because as the mass flow quality increases the liquid phase portion of the multiphase flow decreases and the dominant phase becomes the gas phase which has lower pressure drop compared to liquid phase for the same flow rate. In addition, the figure shows that as the mass flow quality increases, the difference between the models decreases. For mass flow quality of 0.2, the largest pressure drop prediction is 1359.09 Pa based on the model proposed by Saisorn and Wongwises [28] while the lowest pressure drop prediction is 264.64 Pa based on Lee and Lee's model [39]. This is equivalent to 413.5% difference between these two models. However, for mass flow quality of 0.9, the model proposed by Saisorn and Wongwises [28] results in 388.45 Pa and the model proposed by Lee and Lee [39] results in 202.09 Pa pressure drop which is equivalent to 92.2% difference. It should be added that the range of mass flow qualities for the PEM fuel cell application is usually greater than 0.8 as shown in the figure in the inset. For mass flow quality of 0.9, a comparison between Mishima and Hibiki [38], Sun and Mishima [40], English and Kandlikar [37], Zhang et al. [41], and Hwang and Kim [42] with Lee and Lee's model [39] results in 55.91%, 21.34%, 12.82%, 10.29%, and 1.07% difference, respectively. In this comparison, Lee and

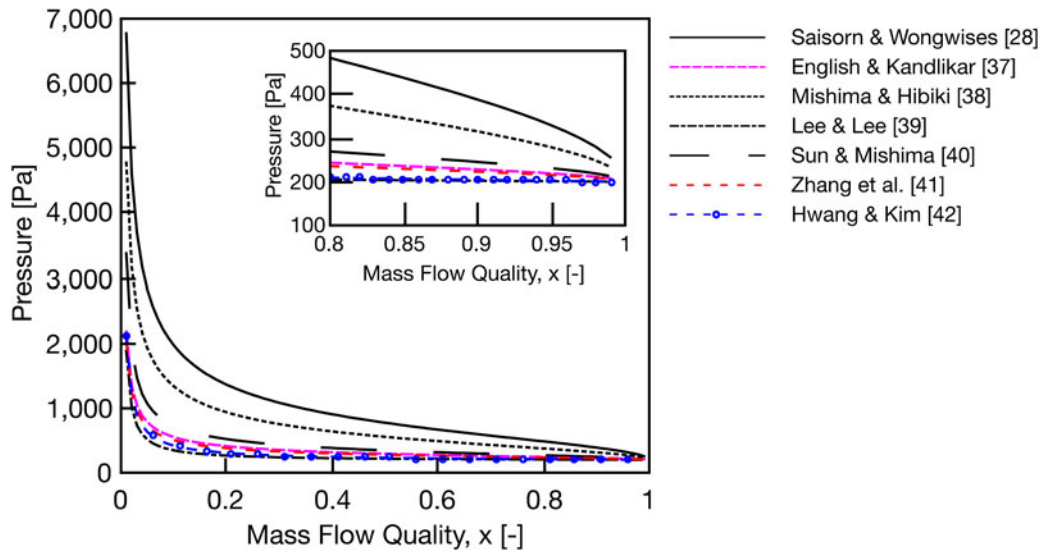


Figure 2. Comparison of two-phase flow pressure drop models evaluated in this study. Calculations are done based on a superficial air velocity of 3.0 m/s.

Lee's model [39] is chosen as the base model because of its lowest pressure drop prediction, which results in positive differences when compared with other models.

Comparing two-phase flow pressure drop models

The experimentally measured two-phase flow pressure drops were compared with nine different models as shown in Figure 3. Of the nine models, seven models were based on the separated flow model (Figure 3a–g), and two models were based on the homogeneous equilibrium model (Figure 3h–i). The horizontal axis of each graph represents the experimentally obtained two-phase flow pressure drop, and the vertical axis represents the predicted two-phase flow pressure drop for each model. A 30% margin for each model is shown with a dashed line. It can be observed from the figure that the separated flow models shown in Figure 3a–g mostly predicted the two-phase flow pressure drop with less than 30% error. However, Figure 3h and i show that the homogeneous equilibrium models demonstrate less prediction capability for the range of air and water flow rates used in this study. Figure 3i significantly over-predicted the two-phase flow pressure drop with more than 50% error. The model introduced by Chen et al. [44] (Figure 3i) was based on large mass flux ranging between 50 and 6000 kg/m²s. This range of mass flux causes much larger inertial forces compared to fuel cell applications. Although the effects of surface tension (σ) and channel hydraulic diameter (D_h) were taken into consideration by incorporating the Weber number and

Bond number into their model, since inertial stresses are not the dominant forces in fuel cell application, the proposed model over-predicted the two-phase flow pressure drop for the flow conditions used in the current study.

The general trend observed in Figure 3 suggests that although separated flow models out-perform homogeneous equilibrium models, they mostly under-predict the two-phase flow pressure drop, especially at lower pressure drops. The only exception is the separated model proposed by Saisorn and Wongwises [28] (Figure 3a) which mostly over-predicted the two-phase flow pressure drop. Four different parameters of λ , ω , θ , and ξ were defined to assess the accuracy of the studied models. The mean absolute percentage error (MAPE) is shown by λ which is determined according to

$$\lambda = \frac{1}{N} \sum \frac{|\Delta P_{F, pred} - \Delta P_{F, exp}|}{\Delta P_{F, exp}} \times 100\% \quad (14)$$

ω , θ , and ξ are defined as the percentage of data points predicted within $\pm 10\%$, $\pm 30\%$, and $\pm 50\%$, respectively. It can be observed from Figure 3 that the model proposed by Mishima and Hibiki [38] showed the best prediction capability with the lowest MAPE value. The superior prediction of this model compared to other models can be attributed to the consideration of the effects of geometry of the tube, using relatively narrower tubing which is closer to the flow channels of PEM fuel cells, using air and water as the working fluid, and considering relatively low superficial fluids velocities, particularly superficial liquid velocity. Figure 4 shows the values of parameter C at different

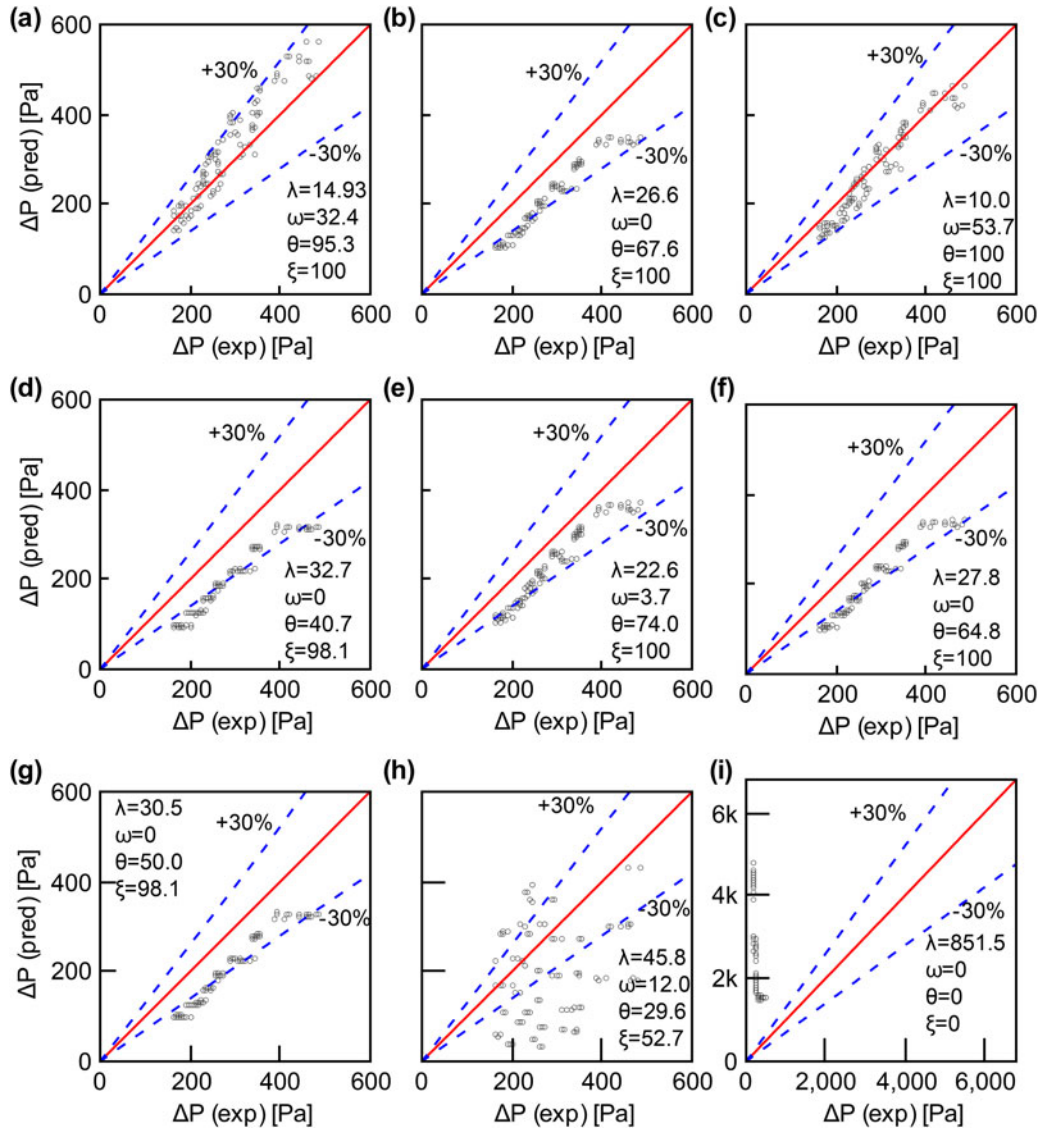


Figure 3. Experimentally measured two-phase flow pressure drops compared with different models. (a) Saisorn and Wongwises [28], (b) English and Kandlikar [37], (c) Mishima and Hibiki [38], (d) Lee and Lee [39], (e) Sun and Mishima [40], (f) Zhang et al. [41], (g) Hwang and Kim [42], (h) Friedel [43], (i) Chen et al. [44]. 108 experimental data points are shown in this figure.

air flow rates, water flow rates, and mass flow qualities. Figure 4a shows the calculated C values at different air flow rates. Different water flow rates were tested at a given air flow rate. Each C value shown in this figure is the average of multiple C values obtained from multiple runs, and the error bars represent the standard deviation between them. The corresponding superficial air velocities for 150 and 500 ml/min were 1.32 and 4.39 m/s, respectively. The general trend in this figure shows that the C values decreased as the air flow rate, and therefore the superficial air velocity, increased. However, the relatively large standard deviation in this figure is an indication of a large variation between C values at different runs at any given air flow rate. Figure 4a also compares the second-order

polynomial curve fitting, shown by the solid line, with C values from Mishima-Hibiki's model [38], shown by the dashed line. The C value from Mishima and Hibiki's model [38] was a function of channel geometry only and did not include the air flow rate and/or the water flow rate. As a result, this model yielded a constant C value at different air flow rates. It can be observed from Figure 4a that the standard deviation of C decreases at higher air flow rates, which indicates a more uniform two-phase flow behavior at higher air flow rates in this study. The findings from Figure 4a suggest that the air flow rate within the channel also influenced the C value and should be included into the model. Figure 4b shows the variation of parameter C at different mass flow qualities and for five different

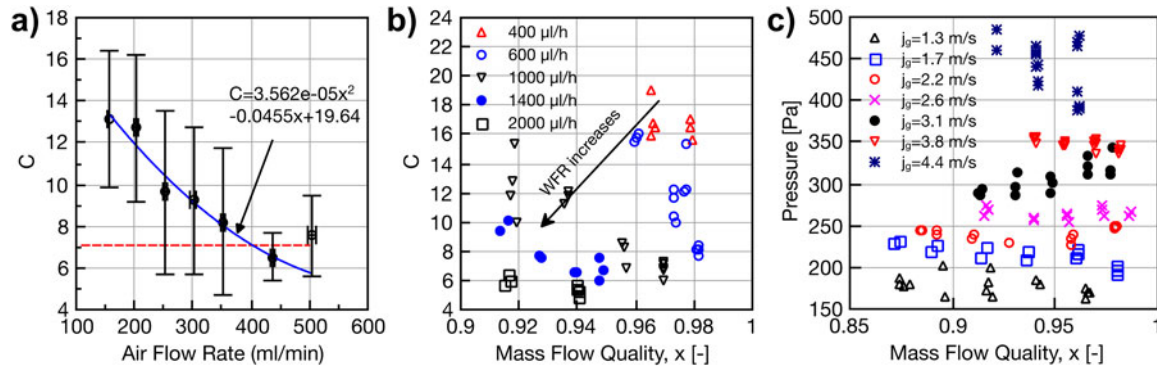


Figure 4. a) C at different air flow rates and all water flow rates considered in this study, x in polynomial fit is the air flow rate in ml/min, the dashed line shows the C value obtained from Mishima-Hibiki model [38] ($R^2 = 0.956$), b) C at different mass flow quantities and different water flow rates. The numbers in the legend show the water flow rates, and (c) two-phase flow pressure drop at different mass flow qualities.

water flow rates. It can be observed from this figure that at a given mass flow quality, values of C decreased as the water flow rate increased. A similar observation was made in an ex-situ study conducted by Grimm et al. [32]. Moreover, Figure 4b shows a reduction in the value of C as the mass flow quality increased for a given water flow rate. For a constant water flow rate, increasing the gas flow rate increased the mass flow quality. Therefore, it can be concluded that the two-phase flow in the PEM fuel cell application is more sensitive to the air flow rate rather than the water flow rate. Furthermore, Figure 4b shows that in addition to the channel geometry, the mass flow quality should also be included in the C correlation.

The variations of the two-phase flow pressure drop based on mass flow quality, x , and superficial air velocity, j_g , are shown in Figure 4c. It can be observed from this figure that for any given superficial air velocity, the two-phase flow pressure drop slightly changed between the lowest and highest mass flow qualities. However, the figure shows that the superficial air velocity had a greater impact on the two-phase flow pressure drop. The increase in pressure drop at a higher superficial air velocity resulted because of the energy dissipation at the moving contact lines. While the figure shows a limited range of mass flow qualities, it covers a relatively large range of water flow rates. For $j_g = 1.3$ m/s, for instance, the water flow rate changed from 400 to 1600 $\mu\text{l/h}$.

The MAPE, defined in Eq. (14), was further studied at different mass flow qualities and superficial air velocities, as shown in Figure 5. The numbers shown in parentheses indicate the number of experiment runs considered to calculate the MAPE at each mass flow quality or superficial air velocity. Figure 5a shows the MAPE at different mass flow qualities for each of

the separated flow models. Other than mass flow qualities $x = 0.87$ and $x = 0.97$, the model proposed by Mishima and Hibiki [38] resulted in the lowest MAPE compared to the other five models. The model proposed by Saisorn and Wongwises [28] showed a smaller MAPE in these two mass flow qualities. Figure 5b shows the MAPE calculated at different superficial air velocities and air flow rates in the flow channel. For superficial air velocities of less than 2 m/s, the model proposed by Saisorn and Wongwises [28] showed a superior performance. However, for superficial air velocities greater than 2 m/s, Mishima and Hibiki's model [38] showed a better prediction capability. The minimum MAPE for this model reached 4.12% for a superficial air velocity around 3.75 m/s. Except for the largest superficial air velocity, the general trend of this figure suggests that the MAPE of all models decreased as the superficial air velocity increased.

Figure 6 shows the two-phase flow pressure drop signatures at five different water flow rates and during the first 8 min of the experiments. The mean value of the pressure drop is shown with a dashed line for each water flow rate. The general trend in all pressure drop signatures indicates an increase in the pressure drop at the beginning of the experiment which is followed by a decrease over time. This can be explained by the acceleration of the liquid plugs up to the velocity of the gas phase within the flow channel. Another observation from this figure indicates that a six-fold increase in water flow rate does not double the mean pressure drop. For constant air flow rate of 300 ml/min an increase in water flow rate from 300 (Figure 6a) to 2000 $\mu\text{l/h}$ (Figure 6e) results in a mean pressure drop increase from 260.9 to 273.8 Pa; this is equivalent to a 5% increase in pressure drop. This insensitivity of the pressure drop to the water flow rate is a result of the tendency of the liquid to wick in

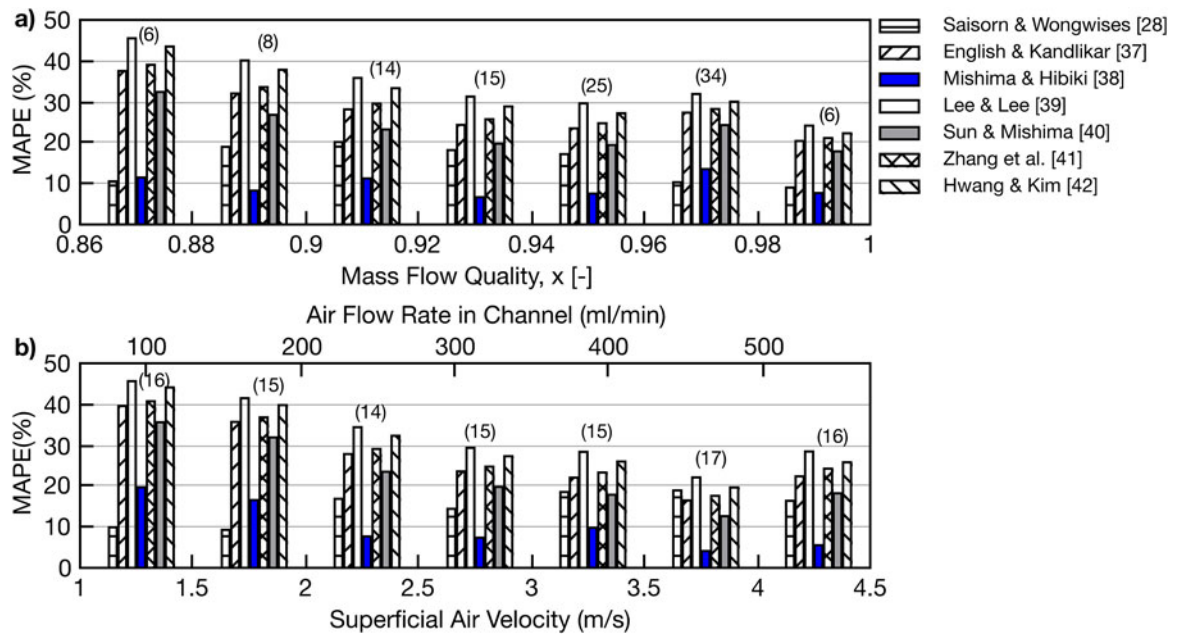


Figure 5. Mean absolute percentage error at (a) different mass flow qualities and (b) different superficial air velocities (bottom axis) and air flow rates (top axis). The numbers in parentheses next to column bars indicate the number of experimental runs considered.

the corner of the hydrophilic flow channel because the contact angle of water on polycarbonate is less than the critical contact angle. The liquid water in the corners of the flow channel provides a lubrication layer for liquid plugs with minimal resistance to the flow. The pressure drop signatures shown in this figure confirm that the experiments were conducted for a sufficient time with no major variation in pressure drop being observed during the last few minutes of the experiments. Comparing the two-phase flow pressure drop signatures at different water flow rates reveals that although the water flow rate has a minor impact on the magnitude of the two-phase flow pressure drop, it affects the time required for the pressure drop signature to reach a uniform trend. For water flow rate of $600 \mu\text{l/h}$, the pressure drop signature reached a uniform trend at minute 4.8 (288 s) while this time reduces to minute 3.5 (210 s) for the $1000 \mu\text{l/h}$ water flow rate, minute 2 (120 s) for the $1400 \mu\text{l/h}$, and minute 1.4 (84 s) for the $2000 \mu\text{l/h}$. Zhao and Bi [49] studied the two-phase flow pressure drop profiles of different flow patterns in minichannels and reported that each two-phase flow pattern had its own unique pressure drop signature. They reported that bubbly flow and churn flow had the minimum and maximum oscillations in pressure drop signature, respectively. As the pressure drop oscillation in Figure 6 is similar for all water flow rates, it can be concluded that the two-phase pattern was the same for the different water flow rates tested.

The pressure drop signatures between minutes 7 (420 s) and 7.55 (453 s) in Figure 6 were further examined in Figure 7. The pressure drop signature for each water flow rate showed periodic cycles which became shorter in time interval as the water flow rate increased. Each cycle started by liquid lobe formation and growth on the tip of the injection capillary and within the flow channel. As the liquid lobe grew in size, the open cross section of the flow channel decreased and the pressure drop increased within the flow channel. The liquid plug entered the flow channel, wicked to the corner of the channel, and transported toward the end of the flow channel with minimal resistance to the shear gas flow. Therefore, the two-phase flow pressure drop profile dropped as shown in the pressure drop signatures. For each water rate, the time interval of one cycle was measured as shown in this figure. For water rate of $600 \mu\text{l/h}$, 13.92 s was required for the pressure drop signature to complete one cycle. This interval was reduced to 5.28 s for the $1000 \mu\text{l/h}$ water flow rate, 3.54 s for the $1400 \mu\text{l/h}$, and 1.2 s for the $2000 \mu\text{l/h}$. However, these time intervals were relative and could change as shown in the pressure drop signature for the water flow rate of $2000 \mu\text{l/h}$ at around 445 s.

Capillary scale two-phase flow

The formation of liquid water and the transport of reactant gases within the flow channels leads to

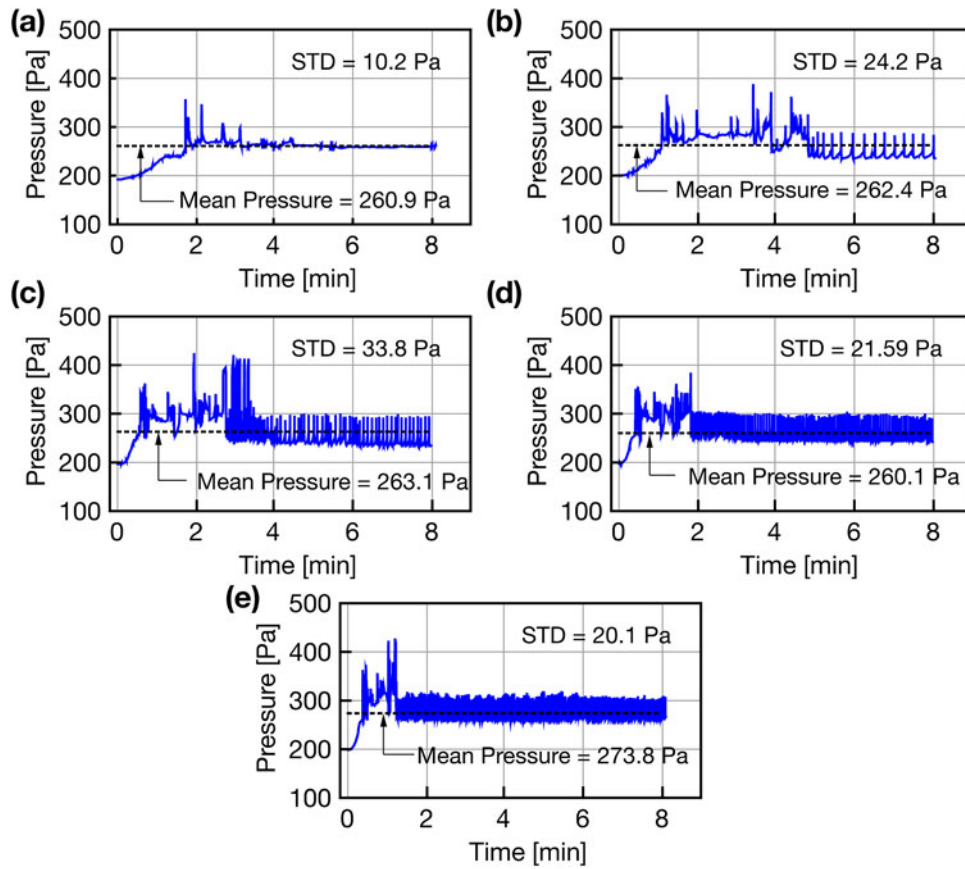


Figure 6. Two-phase flow pressure drop signatures at 300 ml/min air flow rate, equivalent to 2.6 m/s superficial air velocities, and at different water flow rates, (a) 300 $\mu\text{l/h}$, (b) 600 $\mu\text{l/h}$, (c) 1000 $\mu\text{l/h}$, (d) 1400 $\mu\text{l/h}$, and (e) 2000 $\mu\text{l/h}$. Dashed line shows the calculated mean pressure.

liquid-gas two-phase flow in the PEM fuel cell flow channels. The two-phase in PEM fuel cell flow channels is a unique type of flow mainly because of the small length scales associated in PEM fuel cells, the unique liquid water emergence mechanism within the flow channels, and the different surface energies of the channel walls. The small length scales of a PEM fuel cell make it a capillary-scale system, a system at which the Bond number is less than one in normal gravity conditions. In capillary-scale systems, capillary forces define the shape of a static gas-liquid interface. The Bond number is a dimensionless ratio of gravitational to capillary forces on a static liquid surface and is defined as $Bo = (L/L_c)^2$, where L and L_c are the characteristic system length and capillary length, respectively. The characteristic system length for circular and rectangular microchannels are the radius and half of the smallest gap width, respectively. The capillary length is defined as $L_c = \sqrt{\sigma/\rho g}$ which is equal to 2.6 mm for water at 80°C. The typical flow channel of a PEM fuel cell has a rectangular cross section of less than 1 mm on each side, making it a mini-channel according to the classification proposed by Kandlikar and Grande [50]. The other two categories

classified by them are microchannels for channels with hydraulic diameters between 10 μm and 200 μm and conventional channels for channels with hydraulic diameters greater than 3 mm. As the characteristic channel length of a PEM fuel cell is less than the capillary length, the Bond number becomes less than one. Therefore, the two-phase flow in a PEM fuel cell is a capillary-scale flow where the capillary force is dominant compared to the gravitational force.

A complex transport mechanism may occur in a capillary-driven system when water wicks in the corner of the channel. This occurs when there is a continuous gradient in the interface curvature. The necessary condition for water to wick into the corner, known as critical wetting, is that the static contact angle must be less than $\frac{\pi}{2} - \eta$. This condition is known as Concus-Finn and is expressed by $\theta_s < \frac{\pi}{2} - \eta$, where θ_s and η are the static contact angle and the corner half-angle, respectively.

Allen and coworkers [51, 52] studied capillary-scale two-phase flow in small channels and discussed that although different patterns of two-phase flow in mini-channels are defined in literature, the main two categories of two-phase flow in capillary-scale systems are

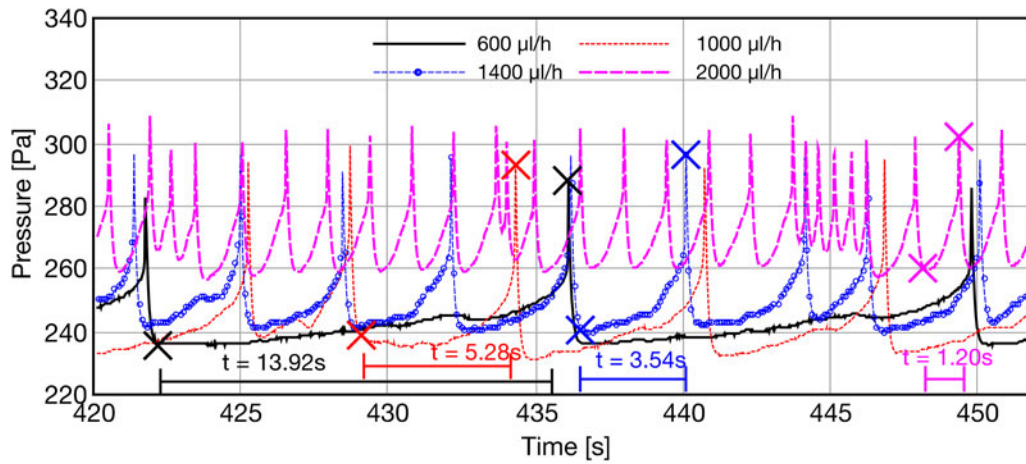


Figure 7. Two-phase flow pressure drop signature at different water flow rates. The numbers in the legend show the water flow rates.

plug flow and annular flow. Plug flow is defined as a flow pattern through which the gas is blocked with plugs of liquid. Plug flow is also referred to as slug flow and happens when the liquid clogs the cross section of the flow channel. In annular flow, however, gas follows through an unimpeded path within the channel. Plug flow usually happens at low capillary and Weber numbers. The capillary number is the ratio of the viscous stress to capillary stress and is defined as $\psi = \mu j_f / \sigma$. The Weber number is the ratio of inertial to capillary stress and is defined as $We = \rho j_f^2 D_h / \sigma$. For Capillary numbers greater than 0.001, viscous effects distort the shape of liquid-gas interface. When the Weber number is greater than 1, inertial effects will begin to break up the liquid-gas surface. Otherwise, the liquid-gas interface is relatively stable at small capillary and Weber numbers.

In conventional channels, the interaction between the liquid and gas phases is inertial. As a result, the two-phase flow pressure drop can be successfully predicted based on the homogeneous equilibrium model and/or the separated flow model. The capillary-scale two-phase flow, however, is dominated by the phenomena that occur over length scales smaller than the Rayleigh instability wavelength, which is typically three times the width, or diameter, of the channel. These phenomena include instability over the gas-liquid interface, contact line dynamics, and menisci motion. While such phenomena occur within small length scales, they can cause significant instabilities over the system. The capillary scale two-phase flow is mainly dominated by the surface tension, contact angle, and geometry of the flow channels. While some models modified the inertial-based phase interaction by considering the surface tension effects [28, 39–41, 44], their prediction capabilities were still not strong

because the channel geometry and contact angle effects were not included. Similarly, capillary-scale two-phase flow is significantly different in square and circular capillaries, because of the superposition of the pressure-driven and capillary-driven flows. Therefore, a successful and universal two-phase flow pressure drop model for minichannels should include the three capillarity properties of surface tension, contact angle, and geometry of a channel.

Conclusions

The liquid-gas two-phase flow pressure drop in a capillary-scale system was measured and compared with the existing models for minichannels. Nine two-phase flow pressure drop models were evaluated for the application of PEM fuel cell. The following conclusions were drawn from this study:

1. Separated flow models showed better prediction capabilities than homogeneous models. However, models based on the separated flow model mostly under-predict the two-phase flow pressure drop.
2. Among the evaluated models, the model proposed by Mishima and Hibiki [38] showed the best prediction capability with an MAPE as low as 4.12% at a superficial air velocity around 3.75 m/s. However, the C correlation proposed by this model only included the geometry of the flow channel and did not include surface tension and surface energy. As discussed in this article, capillary-scale flow is attributed to these three properties, and therefore, a universal model should include the effects of all three.
3. The two-phase flow pressure drop in the minichannels of the test section is more sensitive to

air flow rate than to water flow rate. Under a constant air flow rate, a six-fold increase in water flow rate resulted in only a 5% increase in the mean pressure drop.

4. While most of the two-phase flow pressure drop models don't include air flow rate in their C correlations, findings from experimentally measured two-phase flow pressure drops shown in Figure 4 suggested that both air and water flow rates influence the C value.
5. The MAPE of separated flow models decreases at higher superficial air velocities.
6. The pressure drop signature at different water flow rates initially increases and then decreases over time. Such behavior is explained by the acceleration of the liquid plugs up to the velocity of the gas phase within the flow channel. In addition, although the water flow rate has minimal impact on the magnitude of the two-phase flow pressure drop, it affects the time required for the pressure drop signature to reach a uniform trend. As the water flow rate increases, the time required for the pressure drop signature to reach a uniform trend decreases.

Acknowledgements

Western New England University is gratefully acknowledged for financially supporting this project. The authors also would like to thank Peter Bennett for fabricating the test section used in this study.

Notes on contributors



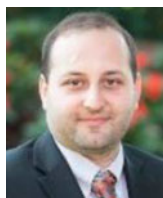
Mehdi Mortazavi is an assistant professor of mechanical engineering at Western New England University, Springfield, MA, USA. He earned his MS and PhD degrees in mechanical engineering from Michigan Technological University in 2011 and 2014, respectively. His research interests

lie at the intersection of multiscale and multiphase flow and transport phenomena, capillary-scale transport phenomena, renewable and sustainable energy systems, and thermal management.



Mahbod Heidari is a postdoctoral fellow and senior researcher in LSCI at Ecole Polytechnique Federale de Lausanne (EPFL) in Lausanne, Switzerland. He received his PhD in energy engineering from EPFL in 2015. His research backgrounds include heat and mass transfer and CFD modeling of boiling and condensation in a novel thermal separation system for desalination

applications, energy storage, optimization of energy systems, and modeling of thermo-fluids systems.



Seyed A. Niknam is an assistant professor of industrial engineering at Western New England University, Springfield, MA, USA. He received his BS degree in mechanical engineering, MS degree in advanced manufacturing systems from Brunel University (UK), and a MS degree in reliability and maintainability engineering from the

University of Tennessee, Knoxville. He earned his doctoral degree in industrial and systems engineering at the University of Tennessee, Knoxville. His research focuses on process control, health monitoring, and statistical signal processing.

References

1. T. V. Nguyen, "Water management by material design and engineering for PEM fuel cells," *ECS Trans.*, vol. 3, no. 1, pp. 1171–1180, 2006.
2. P. Sinha, P. Mukherjee, and C. Wang, "Impact of GDL structure and wettability on water management in polymer electrolyte fuel cells," *J. Mater. Chem.*, vol. 17, no. 30, pp. 3089–3103, 2007. DOI: [10.1039/b703485g](https://doi.org/10.1039/b703485g).
3. A. Bazylak, "Liquid water visualization in PEM fuel cells: A review," *Int. J. Hydrogen Energy*, vol. 34, no. 9, pp. 3845–3857, 2009. DOI: [10.1016/j.ijhydene.2009.02.084](https://doi.org/10.1016/j.ijhydene.2009.02.084).
4. N. Parikh, J. Allen, and R. Yassar, "Microstructure of gas diffusion layers for PEM fuel cells," *Fuel Cells*, vol. 12, no. 3, pp. 382–390, 2012. DOI: [10.1002/fuce.201100014](https://doi.org/10.1002/fuce.201100014).
5. M. Mortazavi, and K. Tajiri, "In-plane microstructure of gas diffusion layers with different properties for PEFC," *J. Fuel Cell Sci. Technol.*, vol. 11, no. 2, pp. 1–9, 2014. DOI: [10.1115/1.4025930](https://doi.org/10.1115/1.4025930).
6. G. Park, Y. Sohn, T. Yang, Y. Yoon, W. Lee, and C. Kim, "Effect of PTFE contents in the gas diffusion media on the performance of PEMFC," *J. Power Sources*, vol. 131, no. 1-2, pp. 182–187, 2004. DOI: [10.1016/j.jpowsour.2003.12.037](https://doi.org/10.1016/j.jpowsour.2003.12.037).
7. J. Ihonen, M. Mikkola, and G. Lindbergh, "Flooding of gas diffusion backing in PEFCs physical and electrochemical characterization," *J. Electrochem. Soc.*, vol. 151, no. 8, pp. A1152–A1161, 2004. DOI: [10.1149/1.1763138](https://doi.org/10.1149/1.1763138).
8. U. Pasaogullari, and C. Wang, "Liquid water transport in gas diffusion layer of polymer electrolyte fuel cells," *J. Electrochem. Soc.*, vol. 151, no. 3, pp. A399–A406, 2004. DOI: [10.1149/1.1646148](https://doi.org/10.1149/1.1646148).
9. A. Bazylak, D. Sinton, and N. Djilali, "Dynamic water transport and droplet emergence in PEMFC gas diffusion layers," *J. Power Sources*, vol. 176, no. 1, pp. 240–246, 2008. DOI: [10.1016/j.jpowsour.2007.10.066](https://doi.org/10.1016/j.jpowsour.2007.10.066).
10. M. Mortazavi, and K. Tajiri, "Liquid water breakthrough pressure through gas diffusion layer of proton exchange membrane fuel cell," *Int. J. Hydrogen Energy*, vol. 39, no. 17, pp. 9409–9419, 2014.

11. A. D. Santamaria, P. K. Das, J. C. MacDonald, and A. Z. Weber, "Liquid-water interactions with gas-diffusion-layer surfaces," *J. Electrochem. Soc.*, vol. 161, no. 12, pp. F1184–F1193, 2014. DOI: [10.1149/2.0321412jes](https://doi.org/10.1149/2.0321412jes).
12. S. G. Kandlikar, E. J. See, M. Koz, P. Gopalan, and R. Banerjee, "Two-phase flow in GDL and reactant channels of a proton exchange membrane fuel cell," *Int. J. Hydrogen Energy*, vol. 39, no. 12, pp. 6620–6636, 2014. DOI: [10.1016/j.ijhydene.2014.02.045](https://doi.org/10.1016/j.ijhydene.2014.02.045).
13. F. Zhang, X. Yang, and C. Wang, "Liquid water removal from a polymer electrolyte fuel cell," *J. Electrochem. Soc.*, vol. 153, no. 2, pp. A225–A232, 2006. DOI: [10.1149/1.2138675](https://doi.org/10.1149/1.2138675).
14. X. Liu, H. Guo, and C. Ma, "Water flooding and two-phase flow in cathode channels of proton exchange membrane fuel cells," *J. Power Sources*, vol. 156, no. 2, pp. 267–280, 2006. DOI: [10.1016/j.jpowsour.2005.06.027](https://doi.org/10.1016/j.jpowsour.2005.06.027).
15. H. Li *et al.*, "A review of water flooding issues in the proton exchange membrane fuel cell," *J. Power Sources*, vol. 178, no. 1, pp. 103–117, 2008. DOI: [10.1016/j.jpowsour.2007.12.068](https://doi.org/10.1016/j.jpowsour.2007.12.068).
16. I. Hussaini, and C. Wang, "Visualization and quantification of cathode channel in PEM fuel cells," *J. Power Sources*, vol. 187, no. 2, pp. 444–451, 2009. DOI: [10.1016/j.jpowsour.2008.11.030](https://doi.org/10.1016/j.jpowsour.2008.11.030).
17. M. Mortazavi, and K. Tajiri, "Effect of the PTFE content in the gas diffusion layer on water transport in polymer electrolyte fuel cells (PEFCs)," *J. Power Sources*, vol. 245, pp. 236–244, January, 2014. DOI: [10.1016/j.jpowsour.2013.06.138](https://doi.org/10.1016/j.jpowsour.2013.06.138).
18. A. M. Schafer, and J. S. Allen, "Improved Water Removal from Fuel Cell Flow Channels via Natural Frequency Excitation of Free Surfaces," *ECS Trans.*, vol. 41, no. 1, pp. 1887–1896, 2011.
19. M. Mortazavi, A. D. Santamaria, J. Z. Benner, and V. Chauhan, "Enhanced Water Removal from PEM Fuel Cells Using Acoustic Pressure Waves," *J. Electrochem. Soc.*, vol. 166, no. 7, pp. F3143–F3153, 2019. DOI: [10.1149/2.0211907jes](https://doi.org/10.1149/2.0211907jes).
20. R. Banerjee, and S. G. Kandlikar, "Liquid water quantification in the cathode side gas channels of a proton exchange membrane fuel cell through two-phase flow visualization," *J. Power Sources*, vol. 247, pp. 9–19, February, 2014. DOI: [10.1016/j.jpowsour.2013.08.016](https://doi.org/10.1016/j.jpowsour.2013.08.016).
21. R. Banerjee, and S. G. Kandlikar, "Experimental investigation of two-phase flow pressure drop transients in polymer electrolyte membrane fuel cell reactant channels and their impact on the cell performance," *J. Power Sources*, vol. 268, pp. 194–203, Dec. 2014. DOI: [10.1016/j.jpowsour.2014.05.123](https://doi.org/10.1016/j.jpowsour.2014.05.123).
22. R. Anderson, E. Eggleton, and L. Zhang, "Development of two-phase flow regime specific pressure drop models for proton exchange membrane fuel cells," *Int. J. Hydrogen Energy*, vol. 40, no. 2, pp. 1173–1185, 2015. DOI: [10.1016/j.ijhydene.2014.11.032](https://doi.org/10.1016/j.ijhydene.2014.11.032).
23. R. Anderson, D. P. Wilkinson, X. Bi, and L. Zhang, "Two-phase flow pressure drop hysteresis in parallel channels of a proton exchange membrane fuel cell," *J. Power Sources*, vol. 195, no. 13, pp. 4168–4176, 2010. DOI: [10.1016/j.jpowsour.2009.12.134](https://doi.org/10.1016/j.jpowsour.2009.12.134).
24. J. Chen, "Experimental study on the two phase flow behavior in PEM fuel cell parallel channels with porous media inserts," *J. Power Sources*, vol. 195, no. 4, pp. 1122–1129, 2010. DOI: [10.1016/j.jpowsour.2009.09.004](https://doi.org/10.1016/j.jpowsour.2009.09.004).
25. S. G. Kandlikar, E. J. See, and R. Banerjee, "Modeling two-phase pressure drop along PEM fuel cell reactant channels," *J. Electrochem. Soc.*, vol. 162, no. 7, pp. F772–F782, 2015. DOI: [10.1149/2.0831507jes](https://doi.org/10.1149/2.0831507jes).
26. A. Kariyasaki, T. Fukano, A. Ousaka, and M. Kagawa, "Characterization of time-varying void fraction in isothermal air-water co-current flow in horizontal capillary tube," *Trans. JSME*, vol. 23, no. 16, pp. 4036–4043, 1991. DOI: [10.1299/kikaib.57.4036](https://doi.org/10.1299/kikaib.57.4036).
27. S. Wongwises, and M. Pipathattakul, "Flow pattern, pressure drop and void fraction of two-phase gas-liquid flow in an inclined narrow annular channel," *Exp. Therm. Fluid Sci.*, vol. 30, no. 4, pp. 345–354, 2006. DOI: [10.1016/j.expthermflusci.2005.08.002](https://doi.org/10.1016/j.expthermflusci.2005.08.002).
28. S. Saisorn, and S. Wongwises, "The effects of channel diameter on flow pattern, void fraction and pressure drop of two-phase air-water flow in circular microchannels," *Exp. Therm. Fluid Sci.*, vol. 34, no. 4, pp. 454–462, 2010. DOI: [10.1016/j.expthermflusci.2009.02.006](https://doi.org/10.1016/j.expthermflusci.2009.02.006).
29. A. Kawahara, P.-Y. Chung, and M. Kawaji, "Investigation of two-phase flow pattern, void fraction and pressure drop in a microchannel," *Int. J. Multiph. Flow*, vol. 28, no. 9, pp. 1411–1435, 2002. DOI: [10.1016/S0301-9322\(02\)00037-X](https://doi.org/10.1016/S0301-9322(02)00037-X).
30. S. Zivi, "Estimation of steady-state steam void-fraction by means of the principle of minimum entropy production," *J. Heat Transf.*, vol. 86, no. 2, pp. 247–252, 1964. DOI: [10.1115/1.3687113](https://doi.org/10.1115/1.3687113).
31. H. Ide, and H. Matsumura, "Frictional pressure drops of two-phase gas-liquid flow in rectangular channels," *Exp. Therm. Fluid Sci.*, vol. 3, no. 4, pp. 362–372, 1990. DOI: [10.1016/0894-1777\(90\)90034-5](https://doi.org/10.1016/0894-1777(90)90034-5).
32. M. Grimm, E. J. See, and S. G. Kandlikar, "Modeling gas flow in PEMFC channels: Part I-Flow pattern transitions and pressure drop in a simulated ex situ channel with uniform water injection through the GDL," *Int. J. Hydrogen Energy*, vol. 37, no. 17, pp. 12489–12503, Jul. 2012. DOI: [10.1016/j.ijhydene.2012.06.001](https://doi.org/10.1016/j.ijhydene.2012.06.001).
33. K. Triplett, S. Ghiaasiaan, S. Abdel-Khalik, A. LeMouel, and B. McCord, "Gas liquid two-phase flow in microchannels: Part II: Void fraction and pressure drop," *Int. J. Multiph. Flow*, vol. 25, no. 3, pp. 395–410, 1999. DOI: [10.1016/S0301-9322\(98\)00055-X](https://doi.org/10.1016/S0301-9322(98)00055-X).
34. R. W. Lockhart, and R. C. Martinelli, "Proposed correlation of data for isothermal two-phase, two-components flow in pipes," *Chem. Eng.*, vol. 45, no. 1, pp. 39–48, 1949.
35. C. Wang, C. Chiang, and D. Lu, "Visual observation of two-phase flow pattern of R-22, R-134a, and R-407C in a 6.5-mm smooth tube," *Exp. Therm. Fluid Sci.*, vol. 15, no. 4, pp. 395–405, 1997. DOI: [10.1016/S0894-1777\(97\)00007-1](https://doi.org/10.1016/S0894-1777(97)00007-1).
36. D. Chisholm, "A theoretical basis for the Lockhart-Martinelli correlation for two-phase flow," *Int. J. Heat*

- Mass Transf.*, vol. 10, no. 12, pp. 1767–1778, 1967. DOI: [10.1016/0017-9310\(67\)90047-6](https://doi.org/10.1016/0017-9310(67)90047-6).
37. N. J. English, and S. G. Kandlikar, “An experimental investigation into the effect of surfactants on air-water two-phase flow in minichannels,” *Heat Transf. Eng.*, vol. 27, no. 4, pp. 99–109, 2006. DOI: [10.1080/01457630500523980](https://doi.org/10.1080/01457630500523980).
 38. K. Mishima, and T. Hibiki, “Some characteristics of air-water two-phase flow in small diameter vertical tubes,” *Int. J. Multiph. Flow*, vol. 22, no. 4, pp. 703–712, 1996. DOI: [10.1016/0301-9322\(96\)00010-9](https://doi.org/10.1016/0301-9322(96)00010-9).
 39. H. L. Lee, and S. Y. Lee, “Pressure drop correlations for two-phase flow within horizontal rectangular channels with small heights,” *Int. J. Multiph. Flow*, vol. 27, no. 5, pp. 783–796, 2001.
 40. L. Sun, and K. Mishima, “Evaluation analysis of prediction methods for two-phase pressure drop in minichannels,” *Int. J. Multiphase Flow*, vol. 35, no. 1, pp. 47–54, 2009. DOI: [10.1016/j.ijmultiphaseflow.2008.08.003](https://doi.org/10.1016/j.ijmultiphaseflow.2008.08.003).
 41. W. Zhang, T. Hibiki, and K. Mishima, “Correlations of two-phase frictional pressure drop and void fraction in mini-channel,” *Int. J. Heat Mass Transf.*, vol. 53, no. 1-3, pp. 453–465, 2010. DOI: [10.1016/j.ijheatmasstransfer.2009.09.011](https://doi.org/10.1016/j.ijheatmasstransfer.2009.09.011).
 42. Y. W. Hwang, and M. S. Kim, “The pressure drop in microtubes and the correlation development,” *Int. J. Heat Mass Transf.*, vol. 49, no. 11-12, pp. 1804–1812, 2006. DOI: [10.1016/j.ijheatmasstransfer.2005.10.040](https://doi.org/10.1016/j.ijheatmasstransfer.2005.10.040).
 43. L. Friedel, “Improved friction pressure drop correlations for horizontal and vertical two-phase pipe flow,” European Two-Phase Group Meeting, Ispra, Italy, Paper E2, 1979.
 44. Y. Chen, K.-S. Yang, and C.-C. Wang, “An empirical correlation for two-phase frictional performance in small diameter tubes,” *Int. J. Heat Mass Transf.*, vol. 45, no. 17, pp. 3667–3671, 2002. DOI: [10.1016/S0017-9310\(02\)00074-1](https://doi.org/10.1016/S0017-9310(02)00074-1).
 45. M. Mortazavi, and K. Tajiri, “Two-phase flow pressure drop in flow channels of proton exchange membrane fuel cells: Review of experimental approaches,” *Renew. Sustain. Energy Rev.*, vol. 45, pp. 296–317, May, 2015. DOI: [10.1016/j.rser.2015.01.044](https://doi.org/10.1016/j.rser.2015.01.044).
 46. C. Hwang *et al.*, “Influence of properties of gas diffusion layers on the performance of polymer electrolyte-based unitized reversible fuel cells,” *Int. J. Hydrogen Energy*, vol. 36, no. 2, pp. 1740–1753, 2011. DOI: [10.1016/j.ijhydene.2010.10.091](https://doi.org/10.1016/j.ijhydene.2010.10.091).
 47. R. K. Shah, and A. L. London, *Laminar Flow Forced Convection in Ducts*. New York: Academic Press; 1978.
 48. J. St-Pierre, “PEMFC in situ liquid-water-content monitoring status,” *J. Electrochem. Soc.*, vol. 154, no. 7, pp. B724–B731, 2007. DOI: [10.1149/1.2737542](https://doi.org/10.1149/1.2737542).
 49. T. Zhao, and Q. Bi, “Co-current air-water two-phase flow patterns in vertical triangular microchannels,” *Int. J. Multiph. Flow*, vol. 27, no. 5, pp. 765–782, 2001. DOI: [10.1016/S0301-9322\(00\)00051-3](https://doi.org/10.1016/S0301-9322(00)00051-3).
 50. S. G. Kandlikar, and W. J. Grande, “Evolution of microchannel flow passages thermohydraulic performance and fabrication technology,” *Heat Transf. Eng.*, vol. 24, no. 1, pp. 3–17, 2003. DOI: [10.1080/01457630304040](https://doi.org/10.1080/01457630304040).
 51. J. S. Allen, “Two phase flow in small channels and the implications for PEM fuel cell operation,” *ECS Trans.*, vol. 3, no. 1, pp. 1197–1206, 2006.
 52. J. Allen, S. Son, and S. Collicot, “Proton exchange membrane fuel cell flow field design for improved water management,” in *Handbook of Fuel Cells*. John Wiley & Sons, New York, NY, 2010.
 53. D. Beattie, and P. Whalley, “A simple two-phase frictional pressure drop calculation method,” *Int J Multiph. Flow*, vol. 8, no. 1, pp. 83–87, 1982. DOI: [10.1016/0301-9322\(82\)90009-X](https://doi.org/10.1016/0301-9322(82)90009-X).